Nanoscale Horizons

ROYAL SOCIETY OF CHEMISTRY

COMMUNICATION

View Article Online
View Journal | View Issue

Cite this: *Nanoscale Horiz.*, 2025, 10, 2873

Received 23rd May 2025,
Accepted 20th August 2025

DOI: 10.1039/d5nh00366k

rsc.li/nanoscale-horizons

Robust dehydrofluorination of HFC-245fa to HFO-1234ze *via in situ* VOFx formation over a non-oxalic acid assisted $V_2O_5/\gamma-Al_2O_3$ catalyst

Fizzah Fatima,[a] Mudadla Umamaheswara Rao,[a] Guo-Ping Chang-Chien,[bcd] Srinivaas Masimukku,[bc] Giridhar Madras,[e] Gedu Satyanarayana[a] and Subrahmanyam Challapalli *[a]

The demand for trans-1,3,3,3-tetrafluoropropene [HFO-1234ze(E)] as a next-generation, low-global-warming-potential (GWP) refrigerant is rising due to international restrictions on high-GWP refrigerants like chlorofluorocarbons (CFCs), hydrochlorofluorocarbons (HCFCs) and hydrofluorocarbons (HFCs). Catalytic dehydrofluorination of HFC-245fa offers a viable synthesis route for the production of HFO-1234ze(E), but the catalyst degradation under harsh acidic conditions remains a major challenge. In this study, a highly stable γ-Al_2O_3 supported catalyst was developed for efficient dehydrofluorination with vanadium species exhibiting the highest activity among the screened metal ions Ni^{2+}, V^{5+}, Zn^{2+}, La^{3+}, Fe^{3+}, Mn^{2+} and Cu^{2+}. The optimized 15 wt% V_2O_5/γ-Al_2O_3 catalyst, prepared without oxalic acid assistance, exhibited strong metal–support interactions and demonstrated superior catalytic performance achieving ~95% HFC-245fa conversion. The catalyst activity increased from 1.3 to 2.1 μmol s^{-1} g_{cat}^{-1} due to the formation of *in situ* VOFx species generated through the interaction between V_2O_5 and HF, as confirmed from NH_3-TPD and XPS analysis. The catalyst also exhibited ~81% selectivity towards HFO-1234ze(E) at 350 °C. It is noteworthy that the catalyst maintained a stable performance up to 74 h, without significant deactivation. Overall, these results highlight the importance of rational metal selection, loading optimization, and interface engineering in developing robust catalysts for industrial hydrofluoroolefin production.

New concepts

The industrial demand for trans-1,3,3,3-tetrafluoropropene [HFO-1234ze(E)] as a next-generation refrigerant has grown significantly due to stringent global regulations on high-global-warming-potential (GWP) substances. This study introduces a novel catalytic approach by incorporating various metal ions into γ-Al_2O_3 to assess their synergistic effects on dehydrofluorination efficiency. Among them, the non-oxalic acid assisted vanadium catalyst demonstrated the most promising catalytic activity. Notably, oxalic acid is commonly used to dissolve ammonium metavanadate in vanadium catalyst synthesis. However, our findings show that it forms bulkier vanadium–oxalate complexes, which hinder vanadium diffusion into the γ-Al_2O_3 support and weaken metal–support interactions, thereby reducing the pore size that leads to low catalytic activity. In contrast, the non-oxalic acid assisted vanadium catalyst exhibited remarkable performance. This key observation underscored the importance of carefully controlling the precursor chemistry to avoid the formation of less active vanadium species. Furthermore, during the dehydrofluorination reaction, an *in situ* transformation occurred, forming vanadium oxyfluoride (VOFx) species from the interaction between V_2O_5 and HF. These VOFx species significantly enhanced the catalytic activity, driving the conversion of HFC-245fa to HFO-1234ze(E). These findings offer valuable insights into designing efficient, durable catalysts for gas-phase dehydrofluorination and highlight the potential for nanoscale control over metal–support interactions to optimize catalytic performance in various industrial applications.

1. Introduction

The rapid acceleration of atmospheric changes and rising global temperature creates an urgent need to develop effective strategies for environmental sustainability. Carbon dioxide (CO_2) is widely recognized as a major contributor to climate change.[1] However, the Intergovernmental panel on climate change (IPCC) report has highlighted the significant role of other chemicals, particularly certain refrigerants. These refrigerants have high global warming potential (GWP) and ozone depletion potential (ODP), exerting a potent and lasting impact on the environment and exacerbating global warming.[2]

In response, the European Union has executed a plan to phase out high ODP and GWP substances like chlorofluorocarbons

[a] *Department of Chemistry, Indian Institute of Technology Hyderabad, Kandi, 502285, Telangana, India. E-mail: csubbu@iith.ac.in*
[b] *Institute of Environmental Toxin and Emerging-Contaminant Research, Cheng Shiu University, Kaohsiung, 833301, Taiwan, Republic of China*
[c] *Super Micro Mass Research and Technology Center, Cheng Shiu University, Kaohsiung, 833301, Taiwan, Republic of China*
[d] *Center for Environmental Toxin and Emerging-Contaminant Research, Cheng Shiu University, Kaohsiung, 833301, Taiwan, Republic of China*
[e] *Department of Chemical Engineering, Indian Institute of Technology Hyderabad, Kandi, 502285, Telangana, India*

(CFCs), hydrochlorofluorocarbons (HCFCs) and hydrofluorocarbons (HFCs) by the end of 2030.[3,4] As a direct consequence, significant research has been directed toward the development of low GWP refrigerants. Among these, hydrofluoroolefins (HFOs) have emerged as promising candidates.[5] In particular, trans-1,3,3,3-tetrafluoropropene [HFO-1234ze(E)] stands out for its favourable properties, including high refrigeration efficiency, compatibility with existing systems and a very low GWP of 6 making it an attractive replacement for traditional fluorocarbons in the pursuit of environmental sustainability.[6]

A recent study demonstrated that HFO-1234ze(E) can be efficiently synthesized *via* the gas-phase dehydrofluorination of 1,1,1,3,3-pentafluoropropane (HFC-245fa), using solid acid catalysts.[7] This reaction involves the cleavage of highly stable C–F bonds, which requires high dissociation energy,[8] necessitating the use of suitable catalysts and elevated reaction temperatures.[9] Therefore, catalyst materials employed in such dehydrofluorination reactions should possess exceptional chemical and thermal stability to endure the corrosive reaction environment.[10]

Catalytic materials including AlF_3,[11] Cr_2O_3[12] and MgF_2[13,14] are widely used in dehydrofluorination reactions. Although AlF_3 demonstrates significant Lewis acidity and initially attains high conversion efficiency (>85%) with moderate selectivity, strong acid sites promote undesirable side reactions and polymerization, resulting in carbon deposition that progressively deactivates the catalyst and compromises the long-term efficiency and stability of the catalyst.[11] To address these issues, metals such as Pd have been introduced as promoters of the AlF_3 catalyst, which helped in reducing coke deposition. However, this significantly increased the overall cost of the catalyst, thereby limiting its practical and large-scale industrial applicability.[15]

Fluorinated Cr_2O_3 and CrF_3 are also active dehydrofluorination catalysts, but their high Lewis acidity leads to coke formation and structural degradation, limiting their long-term stability and practical use.[16,17] To overcome these issues, magnesium fluoride (MgF_2), which possesses moderate Lewis acidity, has been explored as an alternative. However, it suffers from significant sintering at temperatures above 280 °C, resulting in the loss of surface area, pore volume, and ultimately a decline in catalytic stability.[18] Thus, the development of cost-effective, highly effective, and stable catalysts remains a crucial goal.

Among the various potential supports, γ-Al_2O_3 stands out due to its moderate acidity, low cost, high surface area, and excellent thermal and chemical stability that collectively promote efficient catalytical performance.[19–21] These properties make γ-Al_2O_3 a promising alternative to conventional catalysts such as MgF_2 and F–Cr_2O_3. In addition, active components in catalysts have garnered increasing attention due to their synergistic interactions with the support, which also enhance the overall catalytic performance.[22] Previous studies have demonstrated that the incorporation of Cr, La, and V metal ions as active components can significantly improve dehydrofluorination activity.[23–26] Among all, vanadium ions provide medium-strength acidity favourable for dehydrofluorination reactions.[27] In addition to acidity, vanadium existing as monomeric VO^{2+}, polymeric VOx, or crystalline V_2O_5. Monomeric VO^{2+} species, offering limited activity due to low surface coverage, while crystalline V_2O_5 may suffer from low dispersion and reduced accessibility. In contrast, polymeric VOx species, with their mixed-valence states and high surface dispersion, are widely recognized as the most active sites in catalytic systems.[28,29]

The present study focuses on the development of novel catalytic materials for efficient transformation of HFC-245fa to HFO-1234ze(E), aiming for a scalable and economically viable process. γ-Al_2O_3 was selected as the support due to its favourable Lewis acidity and thermal and chemical stability under harsh reaction conditions. To identify an effective active component, a series of metal ions supported on γ-Al_2O_3 were initially screened for dehydrofluorination activity, with vanadium emerging as the most promising candidate. An optimized V_2O_5 loading on γ-Al_2O_3 was subsequently investigated to achieve enhanced catalytic activity and stability. Furthermore, the influence of oxalic acid treatment on the metal–support interaction in V_2O_5/γ-Al_2O_3 catalysts was also explored. These findings provide critical insights into the fundamental aspects of catalytic optimization, paving the way for more efficient and durable dehydrofluorination processes.

2. Experimental

2.1. Chemicals

Commercial γ-Al_2O_3 was purchased from Thermo Scientific and utilized as the support. The metal precursors NH_4VO_3, $(COOH)_2 \cdot 2H_2O$, $Ni(NO_3)_2 \cdot 9H_2O$, $Cu(NO_3)_2 \cdot 3H_2O$ and $La(NO_3)_3 \cdot 6H_2O$ were purchased from Sisco Research Laboratories (SRL). $Zn(NO_3)_2 \cdot 6H_2O$ and $Fe(NO_3)_3 \cdot 9H_2O$ were purchased from AVRA and $Mn(NO_3)_2 \cdot 4H_2O$ was purchased from Sigma. All chemicals used in this study were of analytical grade purity.

2.2. Catalyst synthesis

The preparation process begins by removing adsorbed impurities from the γ-Al_2O_3 support by heating it at 400 °C for 4 h, ensuring the elimination of contaminants. A calculated amount of metal precursor is then added to the support, with metal oxide loading typically ranging from 10 to 20 wt% to optimize catalytic performance. The mixture is stirred for 4 h to facilitate uniform deposition of the metal oxide on the support. Excess water is evaporated at 110 °C, followed by drying at 80 °C for 12 h to remove residual moisture. Finally, the catalyst is calcined at 400 °C for 4 h in a muffle furnace. To evaluate the effect of oxalic acid assistance, the best-performing catalyst was synthesized using a 1 : 2 molar ratio of active metal to oxalic acid, following the same procedure described above.

2.3. Catalyst characterization

The physicochemical properties of the catalysts were determined using a range of characterization techniques. Surface area measurements were conducted using nitrogen adsorption–desorption isotherms at 77 K *via* the Brunauer–Emmett–Teller (BET) method (Quantachrome NOVA 2200e), with samples degassed at 300 °C

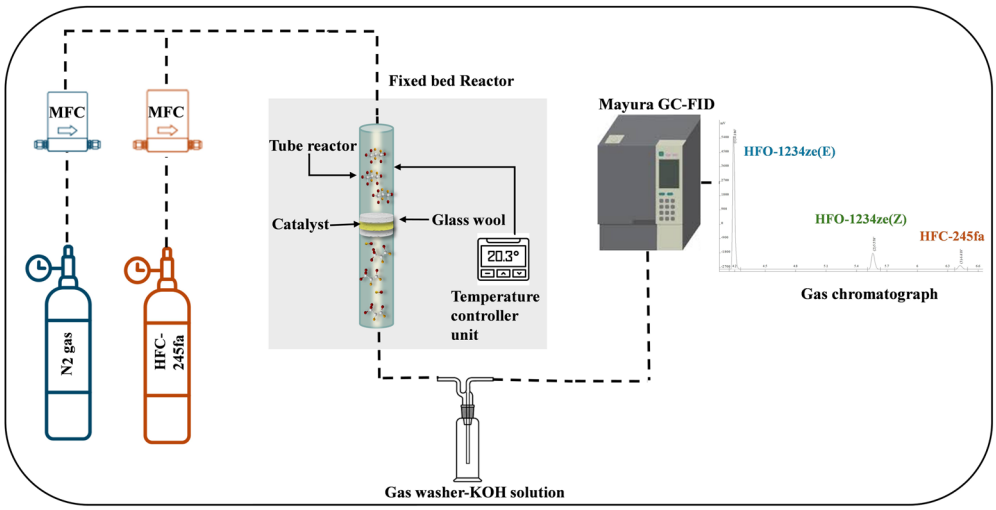

Fig. 1 Schematic diagram of the experimental setup.

for 4 h. Powder X-ray diffraction (XRD) was performed with a PANalytical X'Pert Pro diffractometer with Cu Kα radiation (λ = 1.5406 Å) operated at 45 kV and 40 mA over a 2θ range of 10–80°, to assess crystallinity and phase composition. The acidity and reducibility of the catalysts were evaluated using ammonia temperature programmed desorption (NH_3-TPD) and H_2 temperature-programmed reduction (H_2-TPR) on a Microtrac BEL chemisorption system with a TCD detector. For NH_3-TPD, ~84 mg of catalyst was pretreated at 400 °C in He for 110 min, followed by NH_3 adsorption and desorption up to 800 °C. In H_2-TPR, samples were pretreated at 300 °C under argon for 80 min, and then were reduced in a H_2/He stream up to 800 °C. Surface elemental composition and oxidation states were analyzed using X-ray photoelectron spectroscopy (XPS) with an AXIS Supra-kratos instrument equipped with a monochromatic Al Kα source (1486.6 eV). Functional groups were identified *via* Fourier transform infrared (FTIR) spectroscopy (BRUKER TENSOR II), while pyridine-ATR spectroscopy in the 1400–1700 cm^{-1} range was employed to distinguish Brønsted and Lewis acid sites. Catalysts were exposed to pyridine, equilibrated for 12 h, and heated at 383 K prior to analysis. Raman spectroscopy was conducted by using a WITec confocal Raman microscope alpha 300R series. The wavelength of the excitation laser was 332 nm. Field emission scanning electron microscopy (FE-SEM; JEOL JSM-7800F) and transmission electron microscopy (TEM) were used to observe morphology and dispersion using a JEOL JEM-F20.

2.4. Catalytic testing

As illustrated in Fig. 1, the catalytic performance tests were conducted in a stainless-steel fixed-bed tubular reactor (15 mm inner diameter, 700 mm length) under atmospheric pressure. The gas flow of nitrogen and HFC-245fa was controlled with a mass flow controller (Bronkhorst, Netherland). Prior to the reaction, 1 gram of the synthesized catalyst was loaded into the reactor, covering it with a quartz wool plug and a thermocouple was positioned at the centre of the catalyst bed to monitor the reaction temperature. The catalyst was pretreated under a nitrogen flow (30 mL min^{-1}) at 300 °C for 1 h. After the pretreatment, the nitrogen flow was stopped, and a feed mixture of HFC-245fa and N_2 with a flow ratio of 3 : 10 mL min^{-1} was introduced (total flow rate: 13 mL min^{-1}; GHSV = 780 g mL^{-1} h^{-1}). To remove the HF from by-product, the reaction effluent was passed through an aqueous KOH solution and subsequently analysed using a gas chromatograph (Mayura Analytical Model 1100) equipped with a flame ionization detector (FID) and a GS-GASPRO capillary column (0.32 mm × 60 m).

The conversion of HFC-245fa, product selectivity and catalytic activities (expressed as the apparent rate, r_a) were calculated as defined below using the following equations:

$$\text{Conversion of HFC-245fa (\%)} = \frac{(\text{HFC-245fa})_{in} - (\text{HFC-245fa})_{out}}{(\text{HFC-245fa})_{in}} \times 100 \quad (1)$$

$$\text{Selectivity of HFOs (\%)} = \frac{[i]_{out}}{(\text{HFC-245fa})_{in} - (\text{HFC-245fa})_{out}} \times 100 \quad (2)$$

$$\text{Apparent rate} = \frac{F \times \text{HFC-245fa Conversion}}{\text{mass}_{cat}} \quad (3)$$

where [i] refers to HFO-1234ze(E) or HFO-1234ze(Z), apparent rates are expressed in μmol s^{-1} g^{-1}, with F representing the molar flow rate of HFC-245fa (μmol s^{-1}) and $mass_{cat}$ denoting the catalyst amount in grams.

3. Results and discussion

3.1. Effect of metal ion variation on catalytic performance

Table 1 shows the catalytic performance of the 10 wt% MOx/γ-Al_2O_3 (M = Ni^{2+}, V^{5+}, Zn^{2+}, La^{3+}, Fe^{3+}, Mn^{2+} and Cu^{2+}) catalysts for the dehydrofluorination of HFC-245fa. For pure γ-Al_2O_3 support, HFC-245fa conversion was found to be 24.2% after

Table 1 Catalytic performance of various metal oxides supported on γ-Al_2O_3 at 350 °C

Catalysts	Surface area ($m^2\ g^{-1}$)	Conversion (%) HFC-245fa	Selectivity (%) HFO-1234ze (E)	Activity ($\mu mol\ s^{-1}\ g_{cat}^{-1}$)
γ-Al_2O_3	197	24.2	80.7	0.5
NiO/γ-Al_2O_3	116	16.9	75.2	0.3
V_2O_5/γ-Al_2O_3	192	54.9	81.6	1.2
ZnO/γ-Al_2O_3	249	35.7	79.3	0.7
La_2O_3/γ-Al_2O_3	252	14.7	77.5	0.3
Fe_2O_3/γ-Al_2O_3	241	11.8	78.3	0.2
MnO_2/γ-Al_2O_3	256	23.4	82.4	0.4
CuO/γ-Al_2O_3	233	52.1	81.1	1.1

Data were taken after 5 h of reaction.

5 h, which can be attributed to the limited number of Lewis acidic sites present on the surface. This low conversion suggests that γ-Al_2O_3 alone is not highly effective for catalysing this reaction. The addition of La_2O_3, Fe_2O_3, ZnO, NiO, and MnO_2 suppresses activity due to either strong acidic sites or overall low acidity.[30] However, CuO and V_2O_5 enhance it, despite CuO having higher acidic sites (shown in Table S1), and V_2O_5 showing higher performance due to the polymeric VOx structure that offers superior acid-redox synergy and interaction.[28,29] Among all, trans-HFO-1234ze emerged as the predominant product in the stream as compared to the *cis*-HFO-1234ze isomer. The conversions, selectivity and activity were calculated according to equations (1)–(3). Based on the catalytic performance of all evaluated materials, V_2O_5 was identified as the most effective active component, exhibiting a higher activity of 1.2 $\mu mol\ s^{-1}\ g_{cat}^{-1}$. These findings highlight the effectiveness of vanadium oxide supported on γ-Al_2O_3 as a promising catalyst for the dehydrofluorination reaction.

3.2. Characterization

3.2.1. Structural characterization. The XRD patterns of the fresh catalysts are shown in Fig. 2(a), from which it can be observed that pure γ-Al_2O_3 shows the characteristic diffraction peaks of the cubic phase of alumina (JCPDS no: 10-0425) at 2θ angles of 46.1° and 66.6° corresponding to *hkl* reflections of (400) and (440), respectively. However, as the V_2O_5 loading on γ-Al_2O_3 increased from 10–15 wt%, the intensities of these characteristic peaks decline gradually with no distinct peaks corresponding to crystalline V_2O_5 phases observed. This trend suggests that the incorporation of V_2O_5 into the catalyst structure is effectively dispersed on the γ-Al_2O_3 surface.[30] However, for the 20 wt%V_2O_5/γ-Al_2O_3 catalyst, some peaks intensified at 2θ values of 15.2°, 20.3°, and 56.15° are observed, which are assigned to the crystalline V_2O_5 clusters (JCPDS no. 41-1426).[31,32] This indicates that vanadium is highly dispersed in the 15 wt% V_2O_5/γ-Al_2O_3 catalyst and such dispersion is essential for maintaining high catalytic activity, as it enhances the interaction between the vanadium species and the alumina support, potentially leading to improved performance in catalytic reactions.[33]

The functional groups of the catalysts were further characterized by FTIR spectroscopy, and the results are shown in Fig. 2(b). In the FTIR patterns of γ-Al_2O_3, the broad band at 3700 to 3200 cm^{-1} is characteristic of the –OH stretching vibration associated with hydroxyl groups. The band at 1638 cm^{-1} corresponds to bending vibrations of physically adsorbed water molecules. Additionally, the peak at 1470 cm^{-1} is attributed to water deformation vibrations. The valley between 1000 and 435 cm^{-1} confirms the presence of the γ-phase of Al_2O_3, while the band at 873 cm^{-1} is assigned to Al–O bending vibrations and Al–O–Al bond in the γ-phase generates a band at 670 cm^{-1}.[34,35] In FTIR, vanadium pentoxide (V_2O_5) shows distinct absorption bands at 1020 and 825 cm^{-1} corresponding to the V=O stretching and V–O–V deformation modes, respectively.[36] However, in the case of V_2O_5 supported on γ-Al_2O_3, these characteristic peaks are often not visible. This is due to the overlap of the γ-Al_2O_3 IR absorption bands in the region between 1000 and 435 cm^{-1}, which creates a "valley" in this spectral range, effectively masking the V_2O_5-related features.[37] Despite the absence of these characteristic V_2O_5 bands, evidence for V_2O_5 loading on the alumina surface can still be observed through the changes in the –OH stretching vibration region (typically observed around 3600–3200 cm^{-1}). As the V_2O_5 content on the alumina support increases, the intensity of the –OH stretching band decreases. This reduction in intensity is attributed to the interaction of V_2O_5 with the surface hydroxyl groups of alumina, leading to a decrease in the number of free –OH groups available for detection. This observation serves as

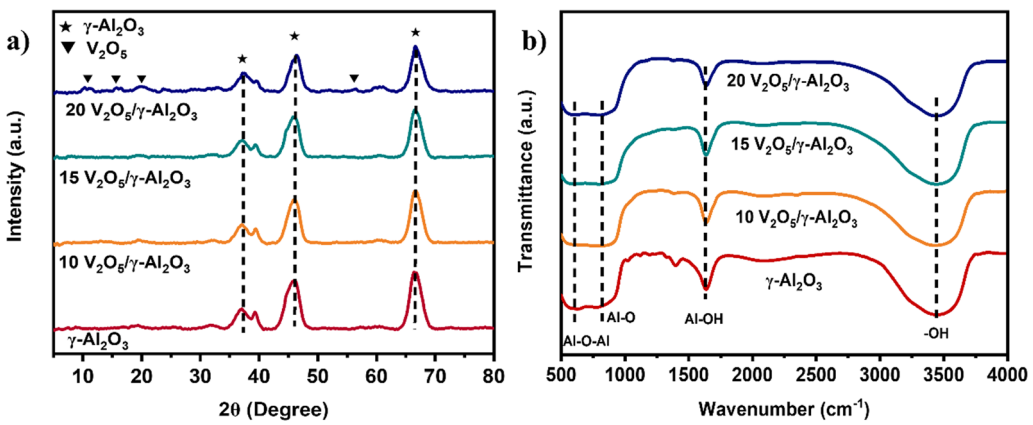

Fig. 2 (a) XRD spectra and (b) FTIR spectra of fresh catalysts.

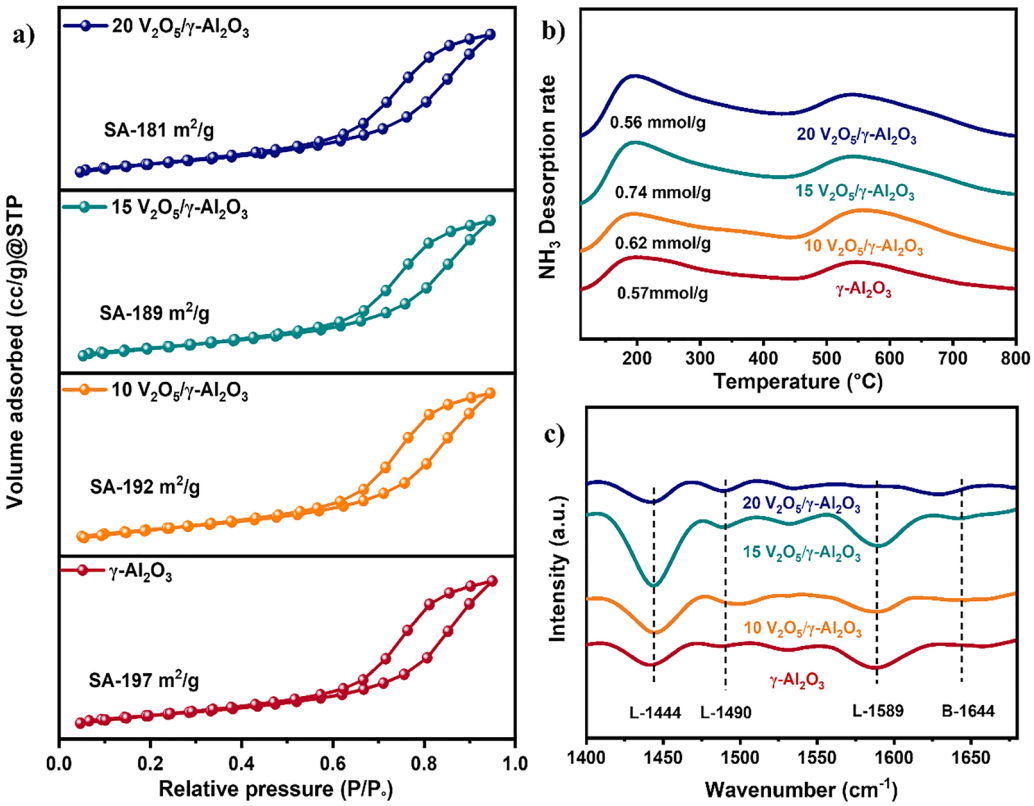

Fig. 3 (a) Nitrogen adsorption–desorption isotherms profiles, (b) NH_3 TPD profiles, (c) and Pyridine-IR profiles of fresh catalysts.

indirect proof of V_2O_5 loading on the alumina surface, highlighting the influence of V_2O_5 on the surface chemistry of the support.[38]

3.2.2. Surface characterization. The nitrogen adsorption and desorption isotherms were determined, and the results are shown in Fig. 3(a). The initial surface area of γ-Al_2O_3 was 197 m^2 g^{-1}. With increasing vanadium loading, the surface area, average pore size, and pore volume decreased, likely due to the deposition of vanadium oxide as shown in Table S2.[39] All catalysts exhibit a Type-IV isotherm with an H3-type hysteresis loop at relative pressures between 0.5 and 0.95, indicating the presence of mesoporous structures. The gradual increase in N_2 adsorption up to a P/P_0 of 0.95 is attributed to multilayer adsorption, rather than distinct monolayer formation.[40]

The surface acidity of the catalysts was measured by NH_3-TPD, and the results are shown in Fig. 3(b). All V_2O_5/γ-Al_2O_3 catalysts exhibit two distinct peaks in the temperature ranges of 100–450 °C and 450–800 °C, which are attributed to weak and strong acidic sites, respectively, as shown in Table S3. A gradual increase in surface acidity was observed with rising vanadium loading on γ-Al_2O_3 from 10–15 wt%, comparative to pure γ-Al_2O_3. This enhancement in acidity is due to the additional acidic sites introduced by the V_2O_5. However, in a series of V_2O_5 from 15–20 wt%, there is a decrease of acidic sites which can be attributed to the agglomeration and crystallization of V_2O_5. These structural changes reduce the availability of active acidic sites, ultimately affecting the catalytic performance.[41] Additionally, the spent 15 wt% V_2O_5/γ-Al_2O_3 catalyst exhibits higher surface acidity (0.957 mmol g^{-1}) compared to the fresh catalyst as shown in Fig. S1(a), suggesting the formation of new species (VOFx), which generate during the reaction between HF and V_2O_5.[42,43]

In Fig. 3(c), the FTIR spectra of pyridine adsorption on the catalysts reveal insightful details about the Lewis and Brønsted surface acidity. All the measured catalysts exhibit characteristic IR bands at 1444, 1490, and 1588 cm^{-1} which are indicative of the presence of Lewis acid sites. In addition, a distinct band at 1640 cm^{-1} is observed, corresponding to Brønsted acid sites, confirming the coexistence of both acid types on the catalyst surface.[44,45] Upon further analysis, the most intense peak is exhibited by Lewis acid sites indicating that Lewis acidity dominates over Brønsted acidity in the catalyst system that are crucial for the dehydrofluorination mechanism. The overall results show that the 15 wt% V_2O_5/γ-Al_2O_3 sample displays the most intense peak of Lewis acidic sites, which contributes to its enhanced catalytic performance in the dehydrofluorination process.

3.2.3. Morphology characterization. Fig. 4 illustrates the morphological and compositional characterization of the synthesized 15 wt% V_2O_5/γ-Al_2O_3 catalyst. SEM analysis depicted in Fig. 4(a & b) shows that the catalyst has irregular and rough surface morphology. Furthermore, the elemental composition of the catalyst was identified through elemental EDX mapping, shown in Fig. 4(c). From the EDX mapping analysis, the catalyst has relative proportions of Al, O and V elements, approximately correlated with the synthesis procedure. Additionally, to examine the particle nature of the catalyst at nanometric scale, TEM

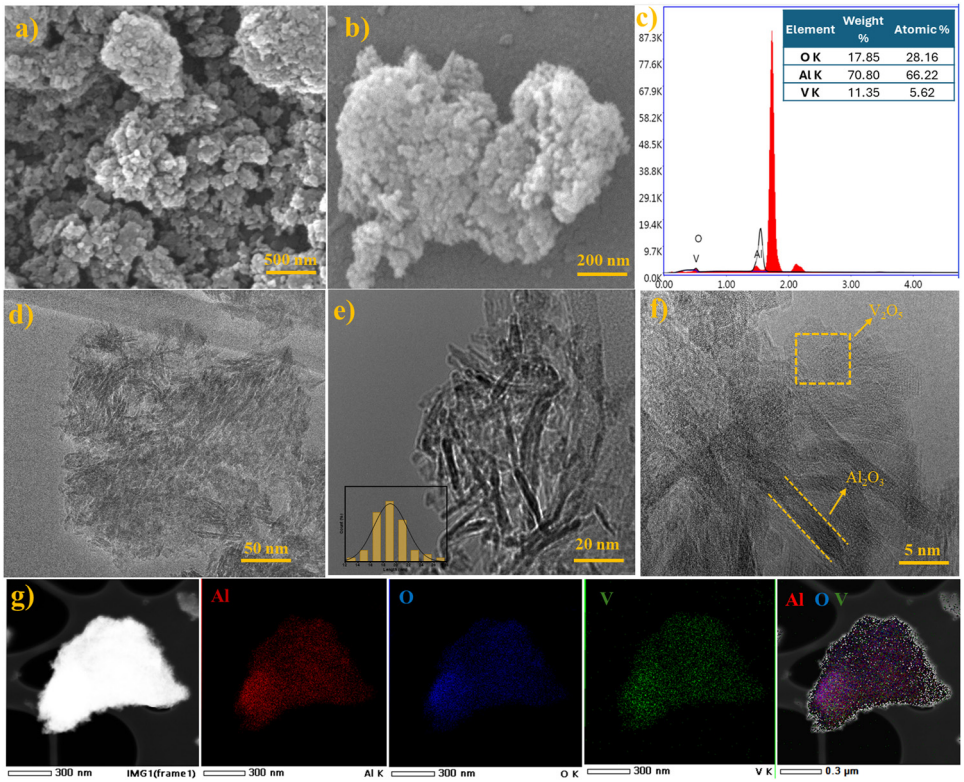

Fig. 4 (a) and (b) SEM morphological analysis, (c) SEM-EDX composition spectrum, (d)–(f) TEM morphological analysis, and (g) STEM-EDX elemental maps of Al, O, and V.

analysis was carried out, revealing a one-dimensional nano sheet and rod morphology (Fig. 4d–f) with an approximate length around 19 nm as evidenced by the histogram.[46] The presence of vanadium on the 15 wt% V_2O_5/γ-Al_2O_3 catalyst was further confirmed by STEM-EDX, as shown in Fig. 4(g). It reveals that Al (red), O (blue) and V (green) homogeneously distributed across the surface of the 15 V_2O_5/γ-Al_2O_3.

3.2.4. Elemental characterization. XPS analysis was performed to investigate the surface chemical states of the catalyst. Fig. 5(a–c) show the deconvoluted spectra of the 15 wt% V_2O_5/γ-Al_2O_3 catalyst, revealing the chemical state of Al, O and V elements, respectively.[47] The Al 2p spectra exhibit features corresponding to Al $2p_{3/2}$ and Al $2p_{1/2}$ peaks in Fig. 5(a). The O 1s spectra, as shown in Fig. 5(b), reveal two types of oxygen species around 531 eV. The peak at a lower binding energy of 530.3 eV is attributed to lattice oxygen, while the peak near 531.7–532 eV corresponds to surface-adsorbed oxygen.[48]

The V 2p XPS spectra of the 15 wt% V_2O_5/γ-Al_2O_3 catalyst reveal an asymmetric peak that deconvoluted into two distinct components, located at binding energies of approximately 516 eV and 517.3 eV in Fig. 5(c). These peaks correspond to vanadium in the V^{3+} and V^{5+} oxidation states, respectively. The presence of V^{3+} species is likely attributed to the partial reduction of surface V_2O_5, which may occur during XPS measurements due to the high vacuum environment and prolonged exposure to X-ray irradiation.[49]

In Fig. 5(d), Raman spectroscopy confirmed the presence of V_2O_5 peaks, with the V–O–V stretching vibration appearing as a broad band in the 750–1000 cm^{-1} regions.[50,51] This broad band is characteristic of the V–O–V stretching modes found in polymeric vanadate. These polymeric structures are often associated with increased catalytic activity, as they can provide a more stable and highly dispersed form of vanadium on the catalyst surface, potentially enhancing the reaction efficiency.[52] The spent 15 wt% V_2O_5/γ-Al_2O_3 catalyst exhibits new Raman bands at 1380 and 1603 cm^{-1} after 78 h of reaction. These Raman bands are characteristic of carbonaceous species, confirming carbon deposition as the main cause of deactivation. This catalyst deactivation is promoted by the surface acidity of the material.[53]

3.3. Effect of vanadium wt% on catalytic performance

The incorporation of vanadium species (V_2O_5) onto γ-Al_2O_3 significantly enhances the catalytic activity, delivering superior performance compared to other metal oxide catalysts. To optimize catalytic efficiency, vanadium loading was systematically varied, aiming to maximize the activity while maintaining catalyst stability and durability throughout the reaction.

Fig. 6(a) shows the catalytic performance of γ-Al_2O_3 and V_2O_5/γ-Al_2O_3 catalysts with varying V_2O_5 loadings (10, 15, and 20 wt%). As the vanadium content increases from 0 to 15 wt%, the HFC-245fa conversion improves from 24.2 to 60%, which is attributed to the increase in the number of available acidic sites. Notably, the catalyst with 15 wt% V_2O_5/γ-Al_2O_3 exhibits a substantial boost in catalytic activity, underscoring the critical role of vanadium loading in enhancing the reaction rate. However, a

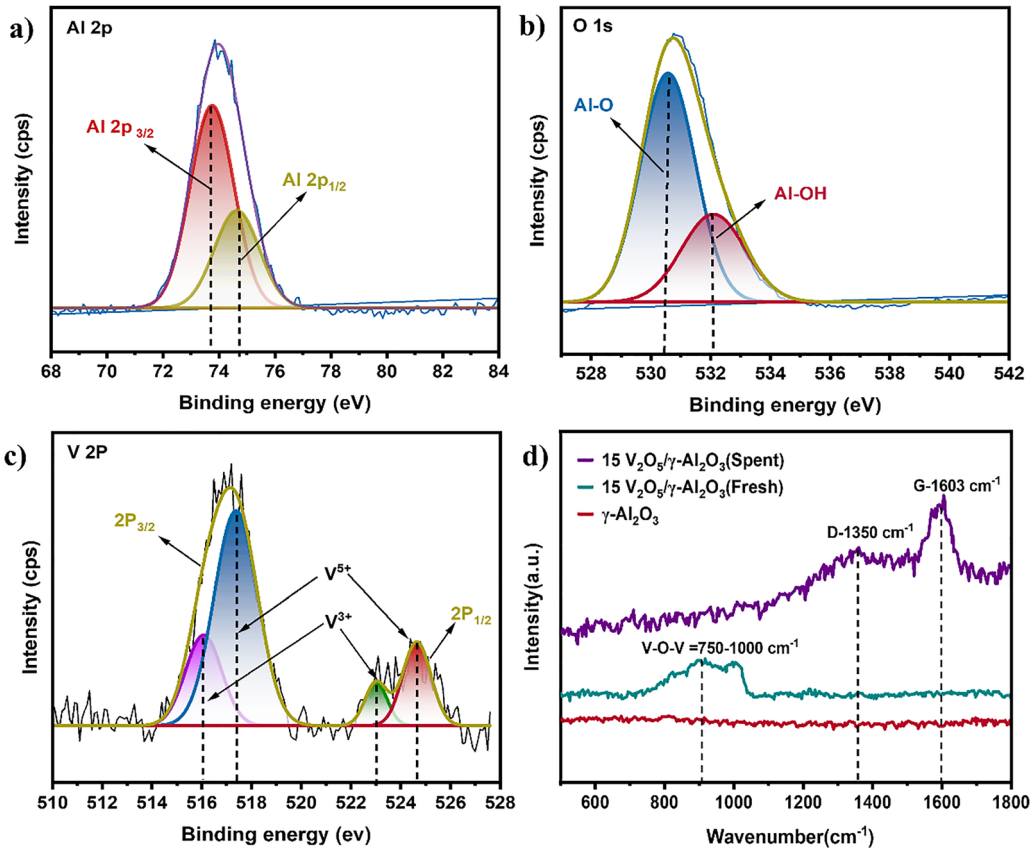

Fig. 5 XPS spectra of (a) Al 2p, (b) O 1s, and (c) V 2p and (d) Raman spectra of the catalyst.

further increase to 20 wt% vanadium results in a sharp decline in conversion, dropping to 30%. This reduction is likely due to the formation of inactive vanadium species, such as crystalline domains or agglomerates, which reduce the number of accessible acid sites and hinder the overall catalytic efficiency.

Further insights into the role of surface acidity were obtained through Fig. 6(b), which shows a linear relationship between the number of acidic sites (μmol g_{cat}^{-1}) and the catalytic activity (μmol s^{-1} g_{cat}^{-1}) of the catalyst. The catalytic activity increases linearly with the number of acidic sites, indicating that the incorporation of V_2O_5 significantly enhances the surface acidity and, consequently, the catalytic performance. Notably, the 15 wt% V_2O_5/γ-Al_2O_3 sample exhibits the highest activity of 1.3 μmol s^{-1} g_{cat}^{-1}. These findings highlight the importance of carefully tuning vanadium loading to optimize the dehydrofluorination reaction.

The effect of reaction temperature on catalyst performance is presented in Fig. 6(c), which shows the catalytic behaviour of the 15 wt% V_2O_5/γ-Al_2O_3 catalyst across a range of reaction temperatures. As the temperature increases from 250 to 400 °C, HFC-245fa conversion rises steadily from 15% to approximately 77%. At lower temperatures (around 250 °C), the conversion remains limited, likely due to insufficient activation energy for C–F bond cleavage in HFC-245fa. However, at 400 °C the conversion rate significantly improves, reaching 77% after 5 h. The marked increase at higher temperatures indicates that elevated thermal energy enhances dehydrofluorination by facilitating reactant activation and improving catalyst activity. Nevertheless, the boost in conversion is accompanied by a slight decline in selectivity for HFO-1234ze(E), decreasing from 81% at 350 °C to 79% at 400 °C. This drop in selectivity could stem from side reactions or coke formation at higher temperatures. Therefore, a balance must be struck between maximizing conversion and maintaining catalyst selectivity and longevity, minimizing the formation of unwanted by-products.[54]

The time-on-stream (TOS) performance of the 15 wt% V_2O_5/γ-Al_2O_3 catalyst at 350 °C over 74 h is shown in Fig. 6(d). An initial induction period during the first 10 h conversion rises sharply from 12 to 70%, eventually stabilizing at ~95%. This trend suggests the progressive formation of new active surface species, such as VOFx that formed *via* surface fluorination of the V_2O_5, which are known to enhance dehydrofluorination activity.[49] The presence of VOFx species was further confirmed by NH_3-TPD and XPS analysis. As shown in Fig. S1(a), the surface acidity increased from 0.704 to 0.957 mmol g^{-1} after the reaction, indicating the formation of additional acidic sites likely due to VOFx. In Fig. S1(b), the XPS analysis of the spent (15 V_2O_5/γ-Al_2O_3) catalyst shows two V $2p_{3/2}$ components of binding energies at 517.3 and 518.4 eV. The component at 517.3 eV is assigned to the V^{5+} species in the catalyst, while the component at 518.4 eV is assigned to V^{n+} species with a much lower electron density. This electron withdrawal from the V

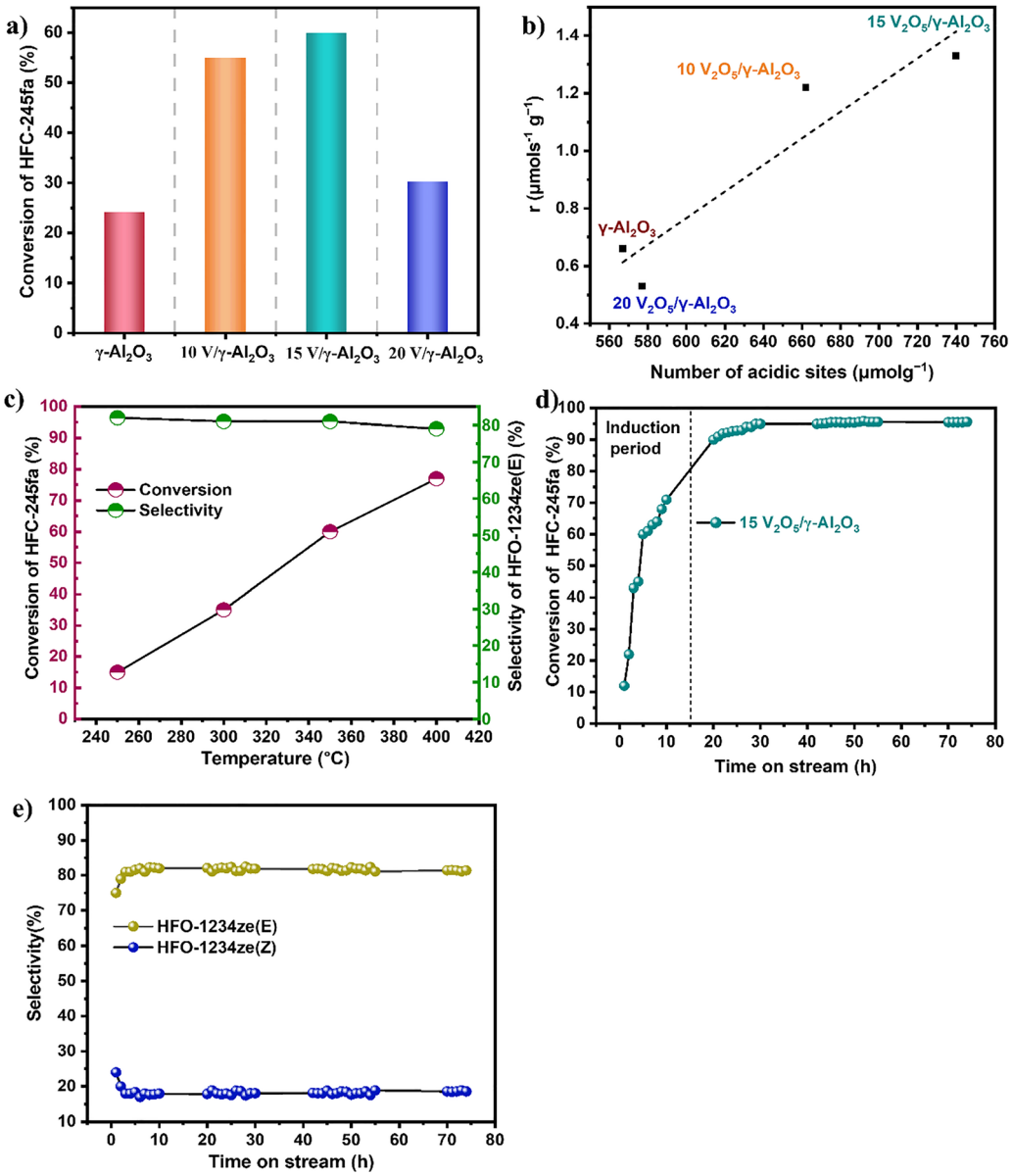

Fig. 6 (a) Conversion performance of various vanadium loadings on γ-Al_2O_3. (b) Correlation between acidic sites and catalytic activity of V_2O_5/γ-Al_2O_3 catalysts with varying loadings. (c) Temperature dependence of catalytic activity for the 15 wt% V_2O_5/γ-Al_2O_3 catalyst. (d) Time-on-stream behaviour of conversion over the 15 wt% V_2O_5/γ-Al_2O_3 catalyst. (e) Time-on-stream behaviour of selectivity of products over the 15 wt% V_2O_5/γ-Al_2O_3 catalyst.

atom is related to the formation of VOFx species, in which the fluorine atoms are much more electronegative and thus extract electrons from vanadium to fluorine. It is due to the reaction between vanadium oxides (most likely V^{5+}) and fluorine-containing compounds (*e.g.*, HF or HFO-1234ze).[26] As a consequence of these transformations, the catalytic activity significantly improved during the reaction, increasing from 1.3 to 2.1 μmol s^{-1} $g_{cat}{}^{-1}$. This enhancement leads to dynamic surface modifications such as the formation of VOFx for maintaining and boosting long-term catalytic performance. A plausible mechanism of HF elimination and VOFx formation over V_2O_5/γ-Al_2O_3 catalysts is illustrated in Fig. S2.

Fig. 6(e) shows the time on stream behaviour of selectivity performance. Throughout the 74 h TOS study, the catalyst maintained consistent selectivity for trans-HFO-1234ze (~81%), with only ~19% selectivity toward the *cis*-isomer. This strong preference can be attributed to the lower Gibbs free energy of formation for the trans-isomer (26.5 kJ mol^{-1} *vs.* 9.5 kJ mol^{-1} for *cis* at 600 K), as supported by thermodynamic analysis.[55] Gas chromatographic profiles shown in Fig. S3(a and b), illustrate the catalyst's behaviour after 5 and 74 h of reaction. The observed increase in conversion over time, along with consistent product distribution, underscores the catalyst's stability and durability under prolonged operating conditions. This consistent performance, as highlighted in Table 2, demonstrates that the catalyst not only maintains high activity but also outperforms previously reported dehydrofluorination systems, establishing it as a potential benchmark in the field.

Table 2 Performance comparison data of previous studies and the present work

S. No.	Catalyst	Temperature (°C)	Conversion of HFC-245fa (%)	Selectivity of HFO-1234ze (*E*)%	Time on stream (h)	Ref.
1	Pd/AlF_3	350	20	81	35	15
2	AlF_3/MOF101	350	95	80	35	41
3	Quasi-MIL-101	350	45	79	25	56
4	NiO/Cr_2O_3	320	79	80	10	23
5	V_2O_5/MgF_2	320	90	81	74	26
6	3V-xFe/MgF_2	300	80	80	50	57
7	MgFe–VO_3-LDH	350	93	80	50	58
8	V_2O_5/γ-Al_2O_3	350	95	81	74	This work

3.4. Effect of oxalic acid-assisted vanadium on catalytic performance

Oxalic acid is widely recognized for its ability to form soluble complexes with metal ions, which can enhance the dispersion and surface interaction of active species with catalyst supports.[59,60] It is also widely studied to prevent particle aggregation and promote uniform surface distribution.[61–63] In particular, it is frequently employed to dissolve precursors such as ammonium metavanadate during the preparation of vanadium-based catalysts.

In this study, we systematically investigated the role of oxalic acid complexion impact on the catalytic performance of the 15 wt% V_2O_5/γ-Al_2O_3 catalyst. The catalytic performance of 15 wt% V_2O_5/γ-Al_2O_3 catalysts with and without oxalic acid assistance is depicted in Fig. (7a). The non-oxalic acid-assisted catalyst achieves ~95% HFC-245fa conversion and maintains stable activity over 74 h. Surprisingly, the oxalic acid-treated catalyst shows a conversion increase over time that confirms the formation of VOFx species, but it reaches a peak conversion up to ~40%, after which it declines rapidly within the first 10 h. Additionally, NH_3-TPD analysis (Fig. 7b) revealed a marked reduction in the number of acidic sites, suggesting a notable alteration of the catalyst's surface properties and a possible decline in surface acidity.

H_2-TPR analysis was also conducted to further investigate the metal–support interactions and the reducibility of the catalyst. As shown in Fig. 7(c), the oxalic acid-assisted 15 wt% V_2O_5/γ-Al_2O_3 (1 : 2 ox) catalyst exhibits a slightly lower temperature reduction peak compared to the catalyst prepared without oxalic acid.

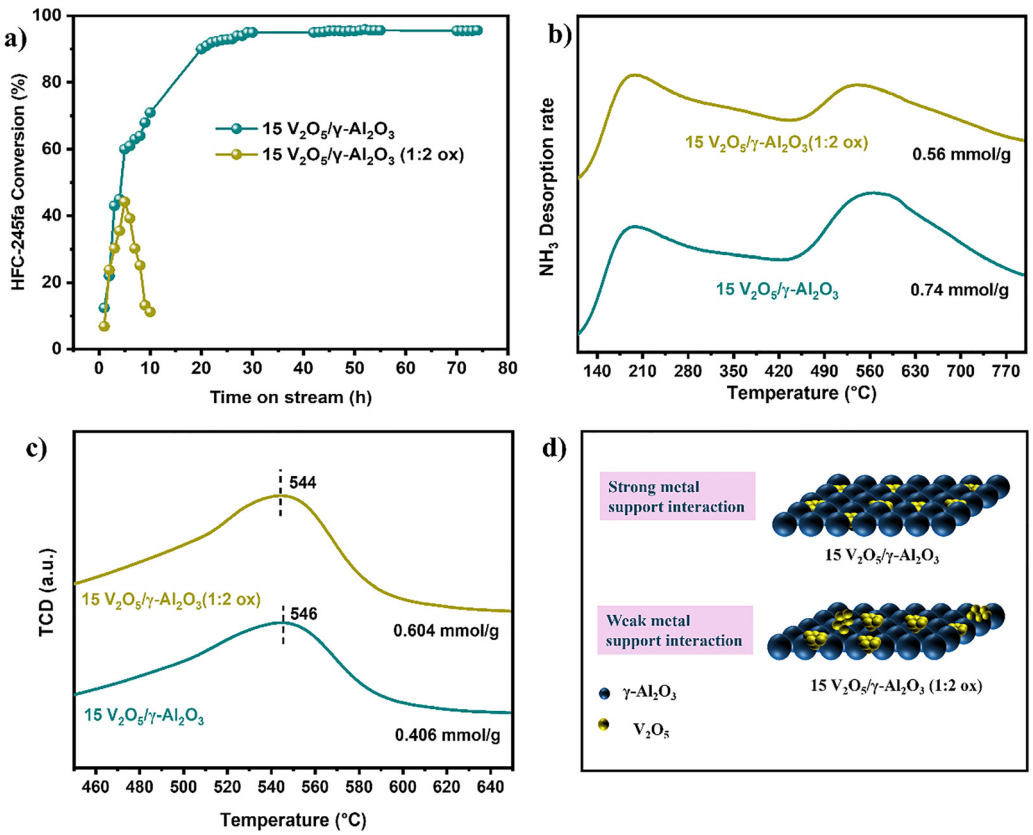

Fig. 7 (a) Conversion performance, (b) NH_3-TPD profile, and (c) H_2-TPR profile of 15 wt% V_2O_5/γ-Al_2O_3 and 15 wt% V_2O_5/γ-Al_2O_3 (1 : 2 ox), (d) Graphical presentation of metal–support interaction.

A reduction peak at a lower temperature typically indicates weaker metal–support interactions, which are often associated with a reduction in the number of active catalytic sites.[64–66] The estimated H_2 consumption for the catalysts prepared without and with oxalic acid assistance was 0.406 and 0.604 mmol g^{-1}, respectively, suggesting notable differences in reducibility and further supporting the inference of weaker metal–support interactions in the oxalic acid-assisted catalyst as illustrated in Fig. 7(d). This weaker interaction likely leads to fewer available acidic sites for the reaction.[67]

The nitrogen adsorption–desorption isotherms were also obtained to evaluate the effect of oxalic acid treatment on the pore size distribution of the catalyst. It was observed that the oxalic acid-treated 15 wt% V_2O_5/γ-Al_2O_3 catalyst exhibited a surface area of 181 m^2 g^{-1} and the pore size distribution was around 3–6 nm diameter, in contrast to the untreated catalyst, which showed 189 m^2 g^{-1}, and the pore size distribution was around 7–8 nm diameter, as shown in Fig. S4(a and b). The researcher found that a small pore size leads to a hindered diffusion of reactant molecules, which in turn promotes coke formation and undesirable side reactions, ultimately leading to catalyst deactivation.[68] Here, the key difference lies in the structural impact of oxalic acid treatment, where the surface chemistry of oxalic acid promotes the formation of vanadium complexes that can play critical roles in weakening metal–support interactions and reducing pore size distribution, thereby diminishing the overall active sites for catalytic dehydrofluorination performance.[69]

Overall, the type of metal ion, its loading percentage, and the strength of the metal support interaction are crucial factors in determining catalytic efficiency and performance. Careful optimization of these parameters is essential to achieve high conversion rates and selectivity in the dehydrofluorination process.

4. Conclusion

This study reported the development of a series of metal oxide catalysts supported on γ-Al_2O_3, incorporating active components such as Ni^{2+}, V^{5+}, Zn^{2+}, La^{3+}, Fe^{3+}, Mn^{2+} and Cu^{2+} for the gas-phase dehydrofluorination of HFC-245fa. Catalytic activity was found to correlate closely with the density of Lewis acid sites. Among these, the optimized 15 wt% V_2O_5/γ-Al_2O_3 catalyst, prepared without oxalic acid assistance, exhibits high surface acidity and strong metal–support interactions demonstrating superior catalytic performance, achieving approximately 95% HFC-245fa conversion and ~81% selectivity towards HFO-1234ze(E) at 350 °C. The progressive improvement in conversion over time is attributed to the formation of new surface VOFx species, generated through the interaction between V_2O_5 and HF, as confirmed from the results of various characterization techniques. Furthermore, no significant catalyst deactivation was observed over 74 h of continuous operation, highlighting the catalyst's excellent stability. These results suggested that the 15 wt% V_2O_5/γ-Al_2O_3 catalyst holds strong potential for industrial applications, particularly in gas-phase dehydrofluorination processes, where long-term durability and minimal degradation are critical for efficient and cost-effective operation.

Author contributions

Fizzah Fatima: methodology, conceptualization, data curation, formal analysis, writing – original draft, and software. Mudadla Umamaheswara Rao: formal analysis, software, investigation, validation, and writing review & editing. Guo-Ping Chang-Chien: methodology, investigation, and writing – review & editing. Srinivaas Masimukku: investigation, methodology, and writing – review & editing. Giridhar Madras: investigation and writing – review & editing. Gedu Satyanarayana: methodology, conceptualization, and funding acquisition. Challapalli Subrahmanyam: conceptualization, supervision, funding acquisition, project administration, and writing – review & editing.

Conflicts of interest

The authors report no declarations of interest.

Data availability

Data will be available from the corresponding author upon request.

Supplementary information is available. See DOI: https://doi.org/10.1039/d5nh00366k

Acknowledgements

Fizzah Fatima sincerely acknowledges Univeristy grant commission, India, for awarding the Junior Research Fellowship to pursue PhD. The authors gratefully acknowledge the financial support for research provided by the Ozone Cell-Ministry of Environment, Forest and Climate Change, Government of India. The authors also extend their gratitude to the Indian Institute of Technology Hyderabad for providing the necessary research facilities.

References

1 H. Luo and X. Liu, *RSC Adv.*, 2024, **14**, 27298–27309.
2 N. Abas, A. R. Kalair, N. Khan, A. Haider, Z. Saleem and M. S. Saleem, Elsevier Ltd, 2018, preprint, 90 (2018) 557–569.
3 Y. Park, N. Shah and B. Gerke, Assessment of commercially available energy-efficient room air conditioners including models with low global warming potential (GWP) refrigerants, 2017. https://www.epa.gov/ozone/ods.html.
4 Significant New Alternatives Policy Program Refrigeration and Air Conditioning Sector Risk Screen on Substitutes for CFC-12, HCFC-22, and R-502 in Retail Food Refrigeration. Substitute: Propane, 2009. https://www.epa.gov/ozone/ods.html.

5 W. Liu, D. Meinel, C. Wieland and H. Spliethoff, *Energy*, 2014, **67**, 106–116.
6 V. Nair, Elsevier Ltd, 2021, preprint, (2021) 156–170.
7 M. Y. Elsheikh and P. D. Tredyffrin, 2000, US6124510.
8 E. Kraka and D. Cremer, *ChemPhysChem*, 2009, **10**, 686–698.
9 H. D. Quan, H. E. Yang, M. Tamura and A. Sekiya, *J. Fluorine Chem.*, 2007, **128**, 190–195.
10 W. Mao, Y. Bai, W. Wang, B. Wang, Q. Xu, L. Shi, C. Li and J. Lu, *ChemCatChem*, 2017, **9**, 824–832.
11 W. Jia, M. Liu, X. Lang, C. Hu, J. Li and Z. Zhu, *Catal. Sci. Technol.*, 2015, **5**, 3103–3107.
12 X. Q. Jia, H. D. Quan, M. Tamura and A. Sekiya, *RSC Adv.*, 2012, **2**, 6695–6700.
13 H. Lee, H. Dam Jeong, Y. Su Chung, H. Gil Lee, M. Jo Chung, S. Kim and H. Sik Kim, 1997, **169**, 307–316.
14 J. K. Murthy, U. Gross, S. Rüdiger and E. Kemnitz, *Appl. Catal., A*, 2004, **278**, 133–138.
15 F. Wang, W. Zhang, Y. Liang, Y. Wang, J. Lu and M. Luo, *Chem. Res. Chin. Univ.*, 2015, **31**, 1003–1006.
16 S. Lima, M. Kim, J. Choia, H. Kima, B. Ahna, S. Leea, H. Leea, C. Kima, D. Suha, J. Haa and K. Song, *Catal. Today*, 2017, **293–294**, 42–48.
17 B. Adamczyk, O. Boese, N. Weiher, S. L. M. Schroeder and E. Kemnitz, *J. Fluorine Chem.*, 2000, **101**(2), 239–246.
18 M. Wojciechowska, Z. Âski and M. Pietrowski, MgF2 as a non-conventional catalyst support 2003, **120**, 1–11.
19 C. J. Breckner, H. N. Pham, M. G. Dempsey, M. A. Perez-Ahuatl, A. C. Kohl, C. N. Lytle, A. K. Datye and J. T. Miller, *Chem. Phys. Chem.*, 2023, **24**, e202300244.
20 A. R. Passos, S. H. Pulcinelli, V. Briois and C. V. Santilli, *RSC Adv.*, 2016, **6**, 57217–57226.
21 A. P. Amrute, K. Jeske, Z. Łodziana, G. Prieto and F. Schüth, *Chem. Mater.*, 2020, **32**, 4369–4374.
22 X. Huang, F. Dong, G. Zhang and Z. Tang, *J. Catal.*, 2023, **420**, 134–150.
23 J. W. Luo, J. D. Song, W. Z. Jia, Z. Y. Pu, J. Q. Lu and M. F. Luo, *Appl. Surf. Sci.*, 2018, **433**, 904–913.
24 W. Mao, B. Wang, Y. Ma, W. Zhang, Y. Du, Y. Qin, J. Kang and J. Lu, *Catal. Commun.*, 2014, **49**, 73–77.
25 M. Jones, G. J. Hutchings, D. J. Willock, J. Scott and S. H. Taylor, *J. Catal.*, 2018, **364**, 102–111.
26 J. D. Song, T. Y. Song, T. T. Zhang, Y. Wang, M. F. Luo and J. Q. Lu, *J. Catal.*, 2018, **364**, 271–281.
27 P. Hu, P. Hu, T. D. Vu, M. Li, S. Wang, Y. Ke, X. Zeng, L. Mai and Y. Long, *Am. Chem. Soc.*, 2023, **123**, 4353–4415.
28 H. Sun, Z. Chen, D. Chen, C. Zhao, Y. Wu, Z. Wu, H. Li, Z. Yuan, Y. Liu, T. Xu, X. Dai and X. Zhang, *Sep. Purif. Technol.*, 2025, **377**, 134188.
29 Z. Lian, L. Liu, C. Lin, W. Shan and H. He, *Environ. Sci. Technol.*, 2022, **56**, 9744–9750.
30 E. P. Reddy and R. S. Varma, *J. Catal.*, 2004, **221**, 93–101.
31 G. Liu, Z. J. Zhao, T. Wu, L. Zeng and J. Gong, *ACS Catal.*, 2016, **6**, 5207–5214.
32 O. Ovsitser and E. V. Kondratenko, *Chem. Commun.*, 2010, **46**, 4974–4976.
33 M. Piumetti, B. Bonelli, P. Massiani, S. Dzwigaj, I. Rossetti, S. Casale, M. Armandi, C. Thomas and E. Garrone, *Catal. Today*, 2012, **179**, 140–148.
34 Z. Gholizadeh, M. Aliannezhadi, M. Ghominejad and F. S. Tehrani, *Sci. Rep.*, 2023, **13**, 6131.
35 W. T. Al-Rubayee, O. F. Abdul-Rasheed and N. M. Ali, *J. Chem.*, 2016, 4683859.
36 K. M. Shafeeq, V. P. Athira, C. H. R. Kishor and P. M. Aneesh, *Appl. Phys. A: Mater. Sci. Process.*, 2020, **126**, 586.
37 C. Santos-Hernández, M. I. Reyes-Valderrama and S. I. Garduño, *Discover Mater.*, 2025, **5**, 54.
38 E. P. Reddy and R. S. Varma, *J. Catal.*, 2004, **221**, 93–101.
39 M. U. Rao, D. Vidyasagar, C. Ghanty, M. Z. Iqbal, K. Bhargavi, P. Ghosal, G. Madras and C. Subrahmanyam, *Ind. Eng. Chem. Res.*, 2024, **63**, 9336–9346.
40 C. Buttersack, *Phys. Chem. Chem. Phys.*, 2019, **21**, 5614–5626.
41 B. Liu, W. Han, A. Chen, L. Li, H. Tang, C. Lu, G. Zhang, Y. Li and X. Li, *Chem. Eng. J.*, 2020, **394**, 124946.
42 C. Socolsky, S. A. Brandán, A. Ben Altabef and E. L. Varetti, *J. Mol. Struct. THEOCHEM*, 2004, **672**, 45–50.
43 M. D. Zidan and A. W. Allaf, *Spectrochim. Acta, Part A*, 2000, **56**, 2693–2698.
44 G. F. Leal, S. Lima, I. Graça, H. Carrer, D. H. Barrett, E. Teixeira-Neto, A. A. S. Curvelo, C. B. Rodella and R. Rinaldi, *iScience*, 2019, **15**, 467–488.
45 H. Song, J. Wang, Z. Wang, H. Song, F. Li and Z. Jin, *J. Catal.*, 2014, **311**, 257–265.
46 L. Samain, A. Jaworski, M. Edén, D. M. Ladd, D. K. Seo, F. Javier Garcia-Garcia and U. Häussermann, *J. Solid State Chem.*, 2014, **217**, 1–8.
47 M. B. Nguyenab, X. Nui Pham and H. V. Doan, *RSC Adv.*, 2021, **11**, 31738–31745.
48 A. Qiao, V. N. Kalevaru, J. Radnik, A. Düvel, P. Heitjans, A. S. H. Kumar, P. S. S. Prasad, N. Lingaiah and A. Martin, *Ind. Eng. Chem. Res.*, 2014, **53**, 18711–18721.
49 J. D. Song, T. Y. Song, T. T. Zhang, Y. Wang, M. F. Luo and J. Q. Lu, *J. Catal.*, 2018, **364**, 271–281.
50 I. E. Wachs and C. A. Roberts, *Chem. Soc. Rev.*, 2010, **39**, 5002–5017.
51 B. L. Hurley, S. Qiu and R. G. Buchheit, *J. Electrochem. Soc.*, 2011, **158**, C125.
52 P. Rosaiah, G. L. Sandhya and O. M. Hussain, *Adv. Sci., Eng. Med.*, 2016, **8**, 83–90.
53 R. Cheruku, D. S. Bhaskaram and G. Govindaraj, *J. Mater. Sci.: Mater. Electron.*, 2018, **29**, 9663–9672.
54 T. Takkawatakarn, S. Praserthdam, S. Wannakao, J. Panpranot and P. Praserthdam, *Sci. Rep.*, 2021, **11**, 8071.
55 H. Yang, S. Wu, Z. Chen, L. Li, H. Wang, B. Liu, H. Tang, Y. Li, A. Chen and W. Han, *Catal. Lett.*, 2021, **151**, 2065–2074.
56 B. Liu, W. Han, X. Li, L. Li, H. Tang, C. Lu, Y. Li and X. Li, *Chem. Eng. J.*, 2020, **394**, 124946.
57 X. X. Fang, W. M. Liao, J. D. Song, W. Z. Jia, Y. Wang, J. Q. Lu and M. F. Luo, *Appl. Surf. Sci.*, 2019, **490**, 365–371.
58 B. Liu, Y. Wang, Y. Huang, L. Liu, Y. Wei, Y. Sun, X. Wei and W. Han, *Appl Catal B*, 2023, **328**, 122477.

59 N. Peys, P. Adriaensens, S. Van Doorslaer, S. Gielis, E. Peeters, C. De Dobbelaere, S. De Gendt, A. Hardy and M. K. Van Bael, *Dalton Trans.*, 2014, **43**, 12614–12623.
60 H. Wang, Y. Fan, G. Shi, H. Liu and X. Bao, *J. Catal.*, 2008, **260**, 119–127.
61 K. Elen, K. Elen, A. Hardy, A. Hardy, M. K. Van Bael and M. K. Van Bael, *J. Chem. Educ.*, 2020, **97**, 1650–1654.
62 V. I. E. Bruyère, L. A. Garcia Rodenas, P. J. Morando and M. A. Blesa, *J. Chem. Soc., Dalton Trans.*, 2001, 3593–3597.
63 J. Chen, Y. Zhang, Z. Zhang, D. Hou, F. Bai, Y. Han, C. Zhang, Y. Zhang and J. Hu, *J. Mater. Chem. A*, 2023, **11**, 8540–8572.
64 S. Li, Y. Fu, W. Kong, J. Wang, C. Yuan, B. Pan, H. Zhu, X. Chen, Y. Zhang, J. Zhang and Y. Sun, *Fuel*, 2023, **343**, 127918.
65 K. Piyapaka, S. Tungkamani and M. Phongaksorn, *Int. J. Appl. Sci. Technol.*, 2016, **9**, 255–259.
66 D. P. Debecker, M. Stoyanova, U. Rodemerck and E. M. Gaigneaux, *J. Mol. Catal. A: Chem.*, 2011, **340**, 65–76.
67 R. Hamidi, R. Khoshbin and R. Karimzadeh, *RSC Adv.*, 2020, **10**, 12439–12450.
68 K. Tian, G. Zhou QinLi, W. Jiang, X. Wang, S. Liu, Y. Zhao and G. Zhou, *RSC Adv.*, 2021, **11**, 11952.
69 J. A. Mendoza Mesa, S. Robijns, I. A. Khan, M. G. Rigamonti, M. L. Bols and M. Dusselier, *Catal. Today*, 2024, 430.

